Critical scaling of whole-brain resting-state dynamics

Adrián Ponce-Alvarez (✉ adrian.ponce@upf.edu)
　Pompeu Fabra University　https://orcid.org/0000-0003-1446-7392

Morten Kringelbach
　University of Oxford　https://orcid.org/0000-0002-3908-6898

Gustavo Deco
　Universitat Pompeu Fabra　https://orcid.org/0000-0002-8995-7583

Article

Critical scaling of whole-brain resting-state dynamics

Adrián Ponce-Alvarez[1*], Morten L. Kringelbach[2,3,4], Gustavo Deco[1,5]

Affiliations
1: Center for Brain and Cognition, Computational Neuroscience Group, Department of Information and Communication Technologies, Universitat Pompeu Fabra, Barcelona 08005, Spain.
2: Department of Psychiatry, University of Oxford, Oxford OX3 7JX, United Kingdom.
3: Center for Music in the Brain, Department of Clinical Medicine, Aarhus University, Aarhus 8000, Denmark.
4: Centre for Eudaimonia and Human Flourishing, Linacre College, University of Oxford, Oxford, UK
5: Institució Catalana de la Recerca i Estudis Avançats (ICREA), Barcelona 08010, Spain.

*Correspondence: adrian.ponce@upf.edu

ORCID numbers: A.P.-A.: 0000-0003-1446-7392; M.L.K.: 0000-0002-3908-6898; G.D.: 0000-0002-8995-7583

ABSTRACT

Scale invariance is a characteristic of neural activity and how it emerges from neural interactions remains a fundamental question. Here, we studied the relation between scale-invariant brain dynamics and structural connectivity by analyzing human resting-state (rs-) fMRI signals, together with diffusion MRI (dMRI) connectivity and its approximation as an exponentially decaying function of the distance between brain regions. We analyzed the rs-fMRI dynamics using functional connectivity and a recently proposed phenomenological renormalization group (PRG) method that tracks the change of collective activity after successive coarse-graining at different scales. We found that brain dynamics display power-law correlations and power-law scaling as a function of PRG coarse-graining. Finally, by studying a whole-brain computational models, we showed that the observed scaling features emerge from critical dynamics and connections exponentially decaying with distance. In conclusion, our study validates the PRG method using large-scale brain activity and theoretical models and suggests that scaling of rs-fMRI activity relates to criticality and the geometry of the brain.

Keywords: Whole-brain structure and dynamics; Scale-invariant dynamics; Renormalization group theory; Criticality

Introduction

Interesting phenomena in biological systems are usually collective behaviors emerging from the interactions among their constituents. Growing evidence indicates that large-scale spontaneous brain activity is an emergent phenomenon continuously generating patterned activity at multiple spatiotemporal scales (Biswal et al., 1995; Fox and Raichle, 2007; Chang and Glover, 2010). How patterned activity arise from the brain's connectivity is a fundamental question in neuroscience. A hallmark of spontaneous, or resting-state (rs), whole-brain activity is scale invariance. Indeed, scale-free (power-law) power spectrum has been reported in human brain dynamics acquired

44   using fMRI (He, 2011; Ciuciu et al., 2011), electrocorticography (He et al., 2010), LFPs (Milstein
45   et al., 2009), and MEG (Dehghani et al., 2010). Moreover, scale-invariance of propagating
46   clusters of activity (*neuronal avalanches*) has been observed in human fMRI recordings
47   (Tagliazucchi et al., 2012), M/EEG fluctuations (Palva et al., 2013; Shriki et al., 2013), and
48   zebrafish whole-brain calcium imaging (Ponce-Alvarez et al., 2018). These works add up to a
49   large body of studies showing scale-invariant neuronal avalanches at the microcircuit level (Beggs
50   and Plenz, 2003; Pasquale et al., 2008; Hahn et al., 2010, 2017; Ribeiro et al., 2010; Friedman et
51   al., 2012).

52
53   In physical systems, scale-invariance is observed at critical points. Thus, the observation of
54   power-law statistics in neural activity has contributed to support the idea that spontaneous neural
55   activity operates close to a phase transition (di Santo et al., 2018). Several studies have shown
56   that critical neural systems maximize information transmission, storage, and processing (Shew et
57   al., 2009; Shew and Plenz, 2013; Marinazzo et al., 2014; Ponce-Alvarez et al., 2018, 2022).
58   Interestingly, it has been shown that brain activity deviates from critical-like behavior in different
59   brain states and neuropsychiatric disorders (Hobbs et al., 2010; Meisel et al., 2012; Hesse and
60   Gross, 2014; Tinker and Velazquez, 2014; Massobrio et al., 2015; Cocchi et al., 2017; Rocha et
61   al., 2022). For instance, awake resting state displays critical-like dynamics, while anesthesia states
62   depart from criticality (Tagliazucchi et al., 2016; Fekete et al., 2018; Ponce-Alvarez et al., 2022).
63   For these reasons it is believed that critical dynamics are a characteristic of healthy, awake
64   spontaneous neural activity.

65
66   Because the critical behavior of a physical system is governed by fluctuations that are statistically
67   self-similar, its statistics are re-scaled after gradual elimination of the correlated degrees of
68   freedom. This is achieved through the Renormalization Group (RG) procedure. This method
69   tracks the change of the joint probability distribution of the system variables after successive
70   coarse-graining at different scales. In the case of critical systems at equilibrium, probability
71   distributions are scale-invariant under iterated coarse-graining and represent fixed points of the
72   RG. In the case of neural activity, to account for the (unknown) topology of interactions, a
73   phenomenological renormalization group (PRG) procedure has been proposed in which
74   maximally correlated variables are group together (Meshulam et al., 2019), instead of locally
75   grouping variables that are spatially close as in most applications of RG. This method successfully
76   revealed scaling features in local single-neuron recordings from the mouse hippocampus
77   (Meshulam et al., 2018, 2019), but remains to be tested at the large scale and using theoretical
78   models.

79
80   Moreover, how the scaling properties of brain dynamics relate to structural principles remains
81   unclear. Previous investigations using retrograde tract tracing methods in mice and nonhuman
82   primates' cortices (Markov et al., 2013; Ercsey-Ravasz et al., 2013; Theodoni et al., 2022) have
83   shown that the probability of a connection existing between two given cortical areas declines with
84   distance. An exponential decay with interareal distance, known as exponential distance rule
85   (EDR), has been proposed as a simple, geometrically-constraint wiring principle (Ercsey-Ravasz
86   et al., 2013; Horvát et al., 2016; Theodoni et al., 2022). Nevertheless, a recent study using
87   fluorescent mapping of neuronal projections found that a power law decay was a marginally better
88   fit than exponential decay (Knox et al., 2018). Special attention has been paid to long-range
89   connections that deviate from simple connection decay as a function of distance, in terms of their
90   impact on wiring-cost (Rubinov et al., 2015) and on dynamics of oscillator models (Choi and
91   Mihalas, 2019; Deco et al., 2021).

92
93   Here, we studied how scale-invariance of brain dynamics relates to structural connectivity. For
94   this, we examined the relation between human rs-fMRI signals and diffusion MRI (dMRI)

2

95   structural connectivity, focusing on spatial anatomical constrains. Next, we studied the scaling
96   properties of rs-fMRI dynamics using the correlation function and the PRG method. Finally, using
97   a simple spin model with a geometrically-constraint connectivity, we showed that scaling in rs-
98   fMRI signals is suggestive of critical behavior.
99
100

Results

Linear prediction of fMRI signals from structural connections

103   We analyzed fMRI signals in a parcellation of $N = 1,000$ regions of interest (ROIs) or nodes. The
104   dataset was composed of 1,003 individual scans of $n_F = 1,200$ time frames. Structural
105   connectivity was obtained using dMRI and probabilistic tractography in the same parcellation,
106   resulting in a $N \times N$ coupling matrix $\boldsymbol{C}$ (see **Methods**) In this section, we studied the relation
107   between fMRI dynamics and structural couplings.

108   We first note that the relation between the connectivity weight between two nodes and the
109   Euclidean spatial distance between those nodes was approximately a power law (**Figure 1A**),
110   indicating the presence of long-range connections. To evaluate the importance of long-range
111   connections, we compared the dMRI connectivity to a model connectivity based on EDR, i.e.,
112    $C_{ij} \propto \exp(-\gamma r_{ij})$, where $r_{ij} = |\vec{x}_i - \vec{x}_j|$, and $\vec{x}_i$ and $\vec{x}_j$ are the positions in 3D space of the
113   centers of ROIs i and j, respectively. Using least squares and for distances < 50 mm, we obtained:
114    $\gamma = 0.106$ mm^{-1}. Notably, the value of γ is consistent with the extrapolation to human brain based
115   on the relation between the EDR and the brain volume (Theodoni et al., 2022). We noted that the
116   EDR fit was higher for intra-hemispheric connections than for the long-range inter-hemispheric
117   ones (**Figure 1B**): the correlation between EDR and dMRI connectivities was equal to 0.69 and
118   0.49 for intra- and inter-hemispheric connections, respectively.

119   We next tested the linear signal prediction of both connectivity matrices. Let $\boldsymbol{X}$ be the $N \times n_F$
120   data matrix containing the fMRI signals. Assuming linear couplings, we calculated the predicted
121   signals as $\boldsymbol{X}_{\text{pred}} = \boldsymbol{CX}$ (i.e., the prediction of each signal given the rest of the network and
122   couplings $\boldsymbol{C}$). The goodness of the linear prediction was given by the Pearson correlation between
123    $X_{\text{pred}}(t)$ and $X(t)$ for all nodes and all subjects. Correlation coefficients were remarkably similar
124   for the dMRI and the EDR, with means equal to 0.51 ± 0.01 and 0.49 ± 0.01, respectively (**Figure
125   1C-D**). These average values were significantly higher (p < 0.001) than the one obtained using a
126   shuffled connectivity that preserves the distribution of dMRI weights but destroys their spatial
127   organization (mean correlation: 0.32 ± 0.01). Consistently, we noted that nodes for which the
128   linear prediction was the lowest were those nodes that were weakly connected to the network (i.e.,
129   nodes with low node strength, **Figure 1E**). We concluded that both the dMRI and the EDR
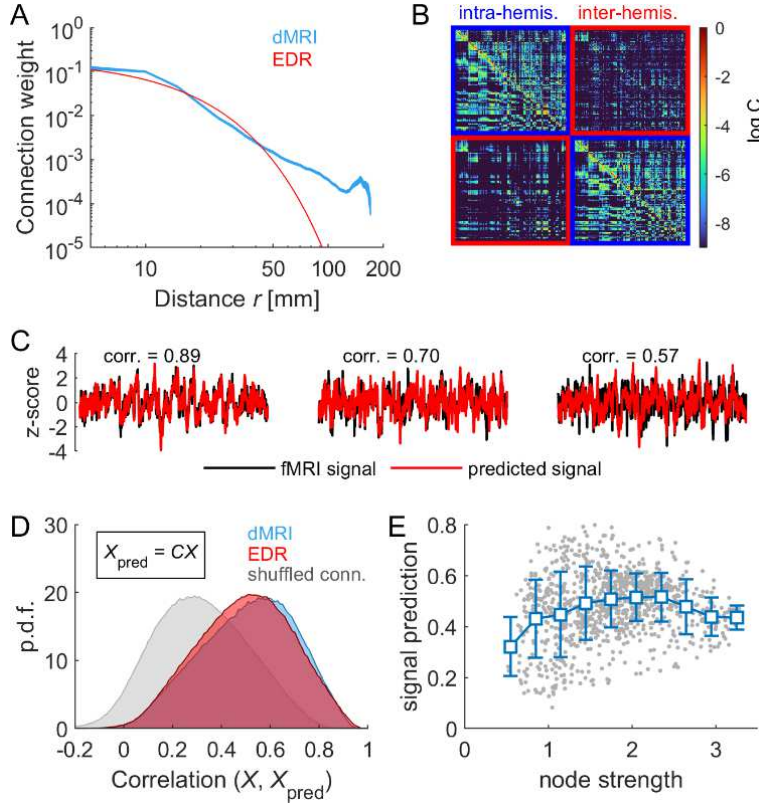130   connectivity matrices were equally good linear predictors of the fMRI signals.

131

Figure 1. Linear prediction of fMRI signals using dMRI and EDR coupling matrices. A) dMRI weights as a function of the distance between pairs of nodes (*blue*) and the exponential approximation (*red*). **B)** Large-scale connectivity. The upper and lower triangular portions of the matrix represent the logarithms of the dMRI and EDR connectivity, respectively. Portions of the matrices corresponding to intra- and inter-hemispheric connections are highlighted in *red* and *blue*, respectively. **C)** Three example fMRI signals and their corresponding linear predictions using the EDR connectivity, i.e., $X_{pred} = CX$. The correlation between the actual and the predicted signals is also indicated. **D)** Distributions of signal predictions using the dMRI connectivity (*blue*), the EDR (*red*), and a shuffled connectivity that preserves the distribution of dMRI weights but destroys the spatial organization (*gray*). **E)** Average signal prediction as a function of the strength of the nodes of the EDR connectivity. Each dot represents a node; the blue trace represents the average relation. Error bars indicate SEM.

Correlation function and phenomenological renormalization-group

We next evaluated the relation $g(r)$ between functional correlations of pairs of ROIs and their distance. As required for the modelling in the next section, we used binarized fMRI signals (see **Methods**). Briefly, for each scan, the z-scored time-series of each ROI, $z_i(t)$ ($1 \leq i \leq N$), was binarized by imposing a threshold $\theta = 1$. Thus, at each time frame t, the collective activity was described by a binary vector $\vec{\sigma} = [\sigma_1, \dots, \sigma_N]$, with $\sigma_i = 1$ if $z_i(t) > \theta$ and $\sigma_i = 0$ otherwise. Binarization of time-series has proven to effectively capture and compress fMRI large-scale collective dynamics (Tagliazucchi et al., 2012; Watanabe et al., 2013; Ponce-Alvarez et al., 2022).

We found that, within a wide range of distances, the average functional correlation, across all ROI pairs and all subjects, was approximately power-law, i.e., $g(r) \sim r^{-\tilde{\eta}}$, with a power exponent equal to $\tilde{\eta} = 0.513 \pm 0.009$ (**Figure 2A-B**). For each individual scan, we tested the power-law hypothesis against an exponential alternative by calculating the ratio between explained variances

159 of least-square fits using the two competing regression models. We found a ratio of ~1.2 of
160 explained variances systematically in favor of the power-law hypothesis (**Figure 2C**). The exact
161 value of the exponent $\tilde{\eta}$ depends on the cutoffs $[r_{\min}, r_{\max}]$ used to constrain the power-law fitting,
162 but for a large region in the $[r_{\min}, r_{\max}]$ plane we found a good fitting of the power law (explained
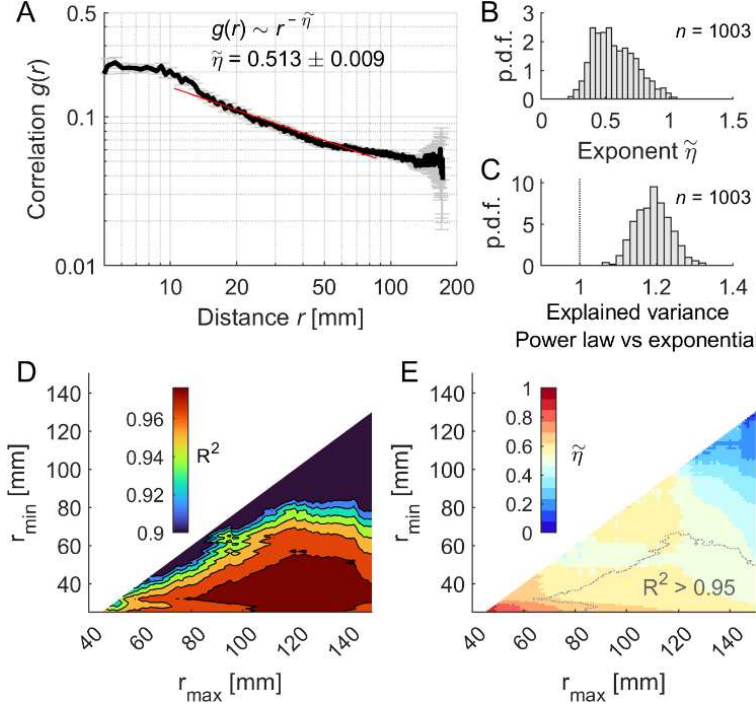163 variance $R^2 > 0.95$) and an exponent around 0.53 (**Figure 2D-E**).

164

165

166 **Figure 2. Correlation function. A)** The correlation function of fMRI signals was approximately power-
167 law, i.e., $g(r) \sim r^{-\tilde{\eta}}$. The power law was fitted in the distance interval $r \in [10, 90]$ mm. **B)** Distribution of
168 the estimated power exponent for single-subject scans. **C)** The power law fit was compared the one obtained
169 using an exponential function by calculating the ratio between the explained variance of the competing
170 regression models. Ratios larger than 1 favors the power law hypothesis. **D-E)** When fitting the power law
171 to $g(r)$ in the distance interval $r \in [r_{\min}, r_{\max}]$, for several combinations of $r_{\min}$ and $r_{\max}$, we found a large
172 region in the $[r_{\min}, r_{\max}]$ plane with high explained variance R^2 (D) yielding power exponents $\tilde{\eta} \sim 0.53$ (E,
173 the gray dotted line indicates the region for which $R^2 > 0.95$).

174

175 Power-law correlations are a hallmark of critical systems, but neither a necessary nor a sufficient
176 condition. Recently, a PRG approach has been proposed to identify scale-invariant activity in
177 neural systems (Meshulam et al., 2019). Within this method, the collective activity is iteratively
178 coarse-grained by grouping maximally correlated variables (see **Methods**). At each coarse-
179 graining step $k = 0, 1, \ldots, k_{\max}$, clusters of size $K = 2^k$ are built, resulting in a system of N/K
180 coarse-grained variables and successively ignoring degrees of freedom. We calculated several
181 observables of the coarse-grained variables and studied their evolution as a function of K.

182 We found that the variance V of coarse-grained variables scaled as a power of the cluster size,
183 i.e., $V \sim K^{\tilde{\alpha}}$, with an average exponent $\langle \tilde{\alpha} \rangle = 1.574 \pm 0.002$ across subjects (**Figure 3A**). This
184 exponent lies in the region between linear ($\tilde{\alpha} = 1$) and quadratic growth ($\tilde{\alpha} = 2$), corresponding
185 to uncorrelated and fully-correlated systems, respectively.

5

Another interesting observable is the probability of silence activity P_{silence}, i.e., time frames in which all signals within a cluster are below their activation threshold. Assuming that the probability distribution of the collective activity in a cluster of size K is a Boltzmann distribution and that the configuration of complete silence has a null energy, $P_{\text{silence}}(K)$ relates to the partition function of the distribution, i.e., $P_{\text{silence}}(K) = Z_K^{-1}$. Thus $\ln P_{\text{silence}}$ can be associated to an effective free energy $F(K) = -\ln Z_K$ (Meshulam et al., 2018). As shown in **Figure 3B**, the effective free energy $F = \ln P_{\text{silence}}$ scales with the cluster size, i.e., $F \sim -K^{\tilde{\beta}}$, with an average exponent $\langle \tilde{\beta} \rangle = 0.673 \pm 0.002$ across subjects.
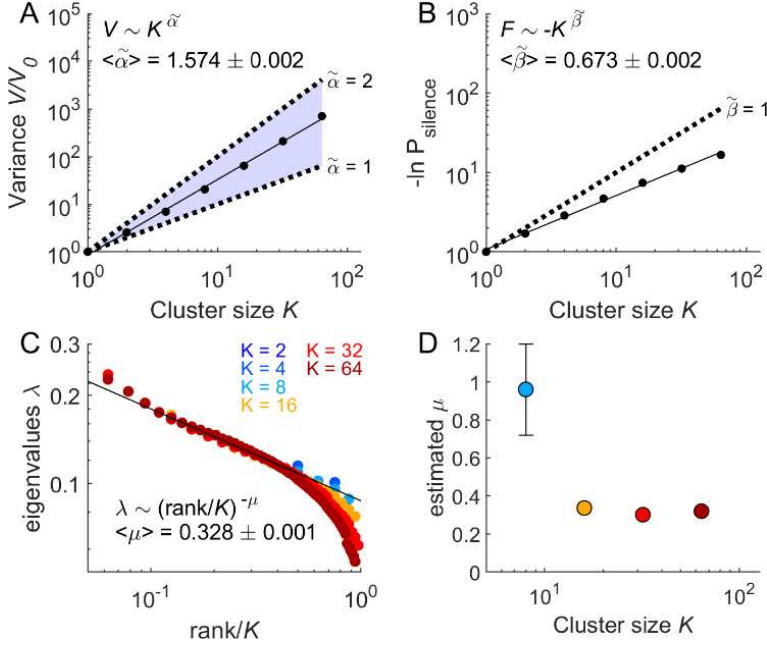

Figure 3. Phenomenological renormalization-group. A) Variance V of coarse-grained variables as a function of cluster size K. The solid black line indicates least squares power law fit, i.e. $V = K^{\tilde{\alpha}}$. Dashed lines indicate linear ($\tilde{\alpha} = 1$) and quadratic ($\tilde{\alpha} = 2$) growths, corresponding to uncorrelated and fully correlated systems, respectively. **B)** Silence log-probability, $F = \ln P_{\text{silence}}$, of coarse-grained variables as a function of cluster size. The solid black line indicates least squares power law fit, i.e. $F = -K^{\tilde{\beta}}$. The dashed line indicates the prediction for uncorrelated variables ($\tilde{\beta} = 1$). In (A) and (B), the variance and the silence log-probability were normalized by their corresponding values at coarse-graining step $k = 0$ (original system). **C)** Eigenvalues λ of the covariance matrix as a function of their relative rank, for clusters of different sizes. The solid black line indicates least squares power law fit, i.e. $\lambda = (\text{rank}/K)^{-\mu}$. **D)** Estimated exponent μ for different cluster sizes. Error bars indicate the estimation error of the exponent (for $K > 8$ error bars are smaller than the symbols).

The last observable that we studied was the eigenvalue spectra of coarse-grained variables. For this, for each cluster of size K, we decomposed the covariance matrix into eigenvectors and studied the behavior of eigenvalues λ as a function of their relative rank (**Figure 3C**). We found a power-law scaling of the eigenvalues as a function of their rank, i.e., $\lambda \sim (\text{rank}/K)^{-\mu}$, with an average exponent $\langle \mu \rangle = 0.328 \pm 0.001$ across subjects. The estimated least-squares exponent μ stabilized for $K > 8$ (**Figure 3D**).

214   In conclusion, using the correlation function and the PRG method we were able to describe the
215   scale invariance of collective fMRI binarized activity by means of four power-law exponents $\tilde{\eta}$,
216    $\tilde{\alpha}$, $\tilde{\beta}$, and μ.

217

Whole-brain spin model

219   To test whether the observed scaling of activity is a signature of criticality, we built a spin model
220   based on large-scale connectivity. The spin model is a canonical model presenting a second-order
221   phase transition between ordered and disordered phases. In this model, at each time step, the state
222   of each node is described by a binary variable, i.e., $\sigma_i \in [-1, +1]$, and the collective activity of
223   the N nodes is given by a binary pattern $\vec{\sigma} = [\sigma_1, \dots, \sigma_N]$. The probability of each pattern is given
224   by the Boltzmann distribution:

$$P(\vec{\sigma}) = \frac{1}{Z}\exp\left(\beta \sum_{i,j} C_{ij}\sigma_i\sigma_j\right), \qquad (1)$$

226   Where $E(\vec{\sigma}) = -\beta \sum_{i,j} C_{ij}\sigma_i\sigma_j$ represents the energy of the pattern; Z is the partition function,
227   i.e., $Z = \sum_{\{\vec{\sigma}\}} \exp(-E(\vec{\sigma}))$; and β is a scaling parameter of the connectivity matrix $\boldsymbol{C}$, equivalent
228   to an inverse temperature, i.e., $\beta = 1/T$, which is the free parameter of the model. The
229   connectivity matrix $\boldsymbol{C}$ was given by the EDR or the dMRI. Realizations of the spin model were
230   obtained using Monte Carlo Metropolis simulations (see **Methods**). For each configuration $\vec{\sigma}$, the
231   population activity is defined as the average node value: $M(\vec{\sigma}) = \sum_i \sigma_i/N$. The average
232   population activity $\langle M \rangle$ was obtained by averaging across simulation steps.

233   For temperatures lower than a critical value, $T_c = \beta_c^{-1}$, the spin model is in an ordered phase and
234   presents a spontaneous population activity (i.e., $|\langle M \rangle| > 0$) that vanishes in the disordered phase
235   for temperatures larger than T_c (**Figure 4A**). Power-law correlation functions were observed at
236   the critical point separating the two phases (**Figure 4B**), with a critical exponent $\tilde{\eta}$ that was close
237   to the one measured in the data for the EDR ($\tilde{\eta} = 0.515 \pm 0.013$; relative error from the empirical
238   exponent: $\Delta_{\tilde{\eta}} = 0.4\%$), but slightly different for dMRI ($\tilde{\eta} = 0.310 \pm 0.009$; $\Delta_{\tilde{\eta}} = 39.6\%$). When
239   fitting a power law to the model correlation function $g(r)$ for the full range of tested temperatures,
240   we found that the power exponent was the closest to the empirical one around the critical point
241   for the two connectivity matrices (**Figure 4C**).

242   We next applied the PRG method to the model activity. We found that, for the EDR and close to
243   the critical point, the scaling of the variance and the covariance eigen-spectrum was similar to the
244   one measured in fMRI data: the critical exponents were equal to $\tilde{\alpha} = 1.62 \pm 0.01$ and $\mu = 0.30 \pm$
245   0.03 ($\Delta_{\tilde{\alpha}} = 2.9\%$, $\Delta_{\mu} = 8.5\%$; **Figures 4D-G**). For the dMRI connectivity, the $\tilde{\alpha}$ critical exponent
246   was similar to the one measured in the fMRI data, but the μ critical exponent deviated from the
247   data: $\tilde{\alpha} = 1.53 \pm 0.05$ ($\Delta_{\tilde{\alpha}} = 2.9\%$) and $\mu = 0.26 \pm 0.02$ ($\Delta_{\mu} = 21.7\%$) (**Figures 4D-G**). Thus,
248   opposite to the case of the EDR, in the case of the dMRI connectivity the empirical exponents
249   could not be simultaneously fitted using a unique temperature parameter. We note that, since spin
250   variables are symmetric (-1 or 1), we cannot define a silence probability to be associated to a free
251   energy. Thus, the exponent $\tilde{\beta}$ could not be calculated for the model.

252   We concluded that, around its critical point, the spin model approximates the fMRI correlations
253   and their scaling features, especially for the EDR, i.e., in the absence of long-range connections.
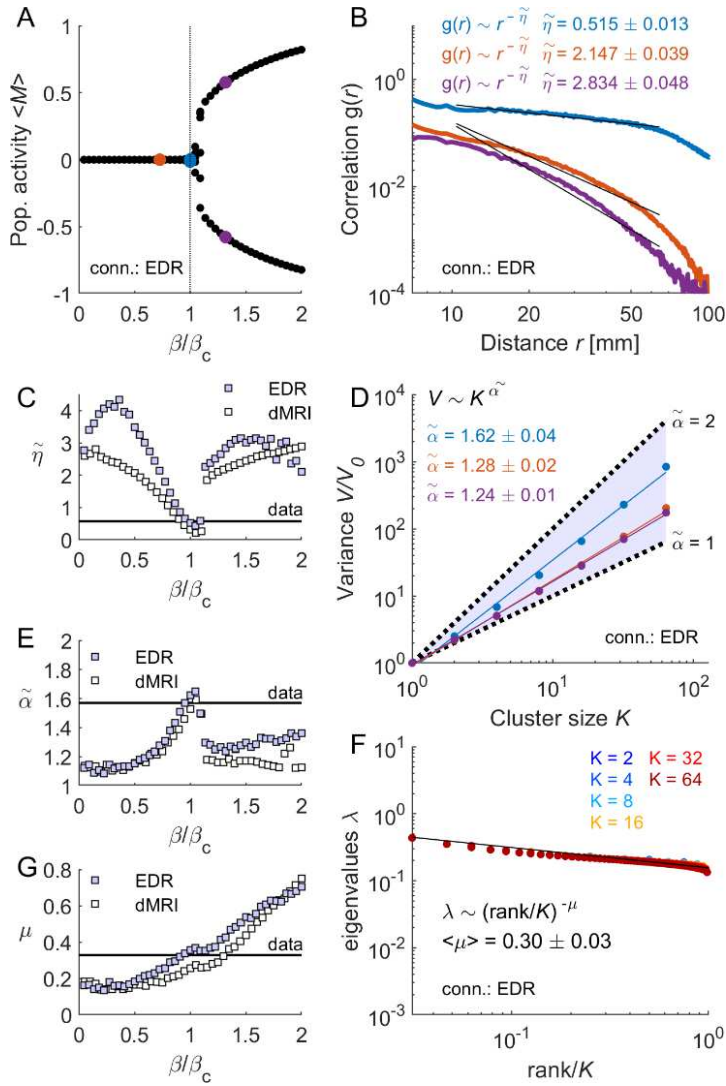
254

Figure 4. Spin model. A) Population activity as a function of $\beta = 1/T$, relative to the critical point $\beta_c = 1/T_c$. For $T > T_c$, the system is disordered and the average population activity is zero. For $T < T_c$, the system is ordered and a spontaneous population activity emerges and settles in either a negative or a positive value (depending on the initial conditions). **B)** At the critical point (*blue*), the correlation function is a power law, with a power exponent $\tilde{\eta}$ close to the one measured in the fMRI data. The correlation function is shown for three example temperatures, also shown in panel (A) (*red*: supercritical; *blue*: critical; *purple*: subcritical). **C)** Exponent $\tilde{\eta}$ as a function of β/β_c. **D)** Variance V of coarse-grained variables as a function of cluster size K, for the three example temperatures. **E)** Exponent $\tilde{\alpha}$ as a function of β/β_c. **F)** Eigenvalues of the covariance matrix as a function of their relative rank, at the critical point, for clusters of different sizes. **G)** Exponent μ as a function of β/β_c. In panels (A), (B), (D) and (F), the connectivity used was the EDR. In panels (C), (E), and (G), the horizontal line indicates the empirically measured exponent.

Discussion

We have shown that rs-fMRI signals present scaling features in the correlation function and as a function of coarse-graining. Notably, we found that the observed scaling can emerge from connections following a simple EDR and critical dynamics, i.e., the scaling exponents observed in the data were strikingly close to those predicted by a critical system of spins interacting through

273 the EDR connectivity. Thus, our results suggest that criticality is the link between the
274 connectome's structure and scale-invariant brain dynamics.

275 Previous theoretical work has tested the PRG method in an interacting particle system, the contact
276 process, and the Ising model, both in a regular 2D lattice and with nearest-neighbor interactions
277 (Nicoletti et al., 2020). The scaling of the contact process and Ising models under PRG yields
278 critical exponents that differ between 3.4-27.2% from those measured from collective neuronal
279 activity of mouse hippocampus, which was the target of those models (Meshulam et al., 2019;
280 Nicoletti et al., 2020). Interestingly, critical exponents in the contact process were found to be
281 unchanged in the presence of long-range interactions in small-world networks (Nicoletti et al.,
282 2020). Our strategy, however, was different since we modeled the system with a proxy of the
283 underlying brain connectivity, thus conserving both the size of the network and the spatial
284 distribution of the nodes. This allowed us to map the scaling exponents observed in rs-fMRI data
285 to the phases of a model presenting a phase-transition. In our case, using the EDR, the model's
286 critical exponents were remarkably close to the exponents measured in rs-fMRI signals (relative
287 error < 8.5%), suggesting that brain dynamics operate close to a critical point in which order and
288 disorder coexist. This result is in line with previous works showing that rs-fMRI signals display
289 critical-like patterned activity detected using other methods, such as neuronal avalanches
290 (Tagliazucchi et al., 2012) and maximum entropy models (Ezaki et al., 2020; Ponce-Alvarez et
291 al., 2022). Since, the EDR has been previously observed in different species (rodents and
292 nonhuman primates), it would be interesting to examine whether large-scale dynamics in these
293 animal models also scale under PRG and relate to criticality.

294 Overall, our study shows that combination of PRG, connectomes, and models can be useful to
295 distinguish the working regime of the observed neural system. Since different behavioral and
296 pathological brain states deviate from critical dynamics (Hobbs et al., 2010; Meisel et al., 2012;
297 Hesse and Gross, 2014; Tinker and Velazquez, 2014; Massobrio et al., 2015; Tagliazucchi et al.,
298 2016; Cocchi et al., 2017; Fekete et al., 2018; Ponce-Alvarez et al., 2022; Rocha et al., 2022),
299 extending these analyses to different brain states could provide new insights on phase transitions
300 in neural systems. We hypothesize that the PRG exponents change depending on the brain state
301 and could be used as biomarkers in clinical and fundamental research. Indeed, in a recent study,
302 Rocha et al. (2022) have shown that criticality is lost in the case of stroke lesions, but it is
303 recovered over time as behavior improves. Thus, criticality signatures can represent promising
304 tools for translational research. Furthermore, we note that the PRG method can be formalized
305 using different interaction measures (e.g., synchrony) and in Fourier space (Meshulam et al.,
306 2019), which makes it suitable to study oscillatory dynamics recorded using LFPs, MEG, or
307 electrocorticography.

308 The dMRI is a non-invasive method to estimate the large-scale brain connectivity, but it has
309 methodological caveats and limitations (Sotiropoulos and Zalesky, 2019). In particular, it
310 estimates short-range intra-hemispheric connections more reliably than inter-hemispheric ones.
311 On the contrary, at the mesoscale, invasive chemical tracers are considered to be the gold standard
312 for estimating the connecting fibers with high accuracy. This technique has shown that connection
313 strength exponentially declines with distance. Here, we showed that dMRI connectivity can be
314 approximated with the EDR with a characteristic scale that was consistent with the extrapolation
315 to human brain given its volume (Theodoni et al., 2022), achieving a good linear prediction of
316 fMRI signals, and yielding an accurate, consistent prediction of scaling exponents of brain activity
317 using a critical whole-brain model. Similarly, the whole-brain model constraint with the dMRI
318 connectivity was able to fit the exponent the coarse-grained variance ($\tilde{\alpha}$) around the critical point,

but the model's correlation function and covariance eigen-spectrum at the critical point were flatter than the empirical functions (i.e., lower exponents μ and $\tilde{\eta}$; see **Figure 4C,G**). We concluded that, at least within the framework of our simple model, the EDR-based critical spin model represents a more parsimonious description of the observed rs-fMRI dynamics than the model based on dMRI connectivity (which presents long-range connections departing from the EDR).

In conclusion, we have shown that whole-brain dynamics display scaling properties that emerge from exponentially decaying connections and critical dynamics, which are two features of connectivity and dynamics largely supported by fiber-tracking research and studies of neural activity at different scales and with different techniques.

Author contributions

A.P.-A. and G.D. designed the research. A.P.-A., M.L.K. and G.D. analyzed/processed data. A.P.-A. designed and performed model analysis and wrote the manuscript.

Declaration of interests

The authors declare no competing interests.

Methods

Materials availability

We used a publicly available dataset of fMRI data from the Human Connectome Project (HCP), from 1003 participants selected from the March 2017 public data release from the Human Connectome Project (HCP). The HCP dataset is available at https://www.humanconnectome.org/study/hcp-young-adult. The code to perform the PRG will be available in a public repository.

Neuroimaging ethics

The Washington University–University of Minnesota (WU-Minn HCP) Consortium obtained full written informed consent from all participants to study procedures and data sharing outlined by HCP, and research procedures and ethical guidelines were followed in accordance with Washington University institutional review board approval.

Functional MRI data

The participants were scanned on a 3T connectome-Skyra scanner (Siemens). We used one rs-fMRI acquisition of approximately 15 minutes, with eyes open and relaxed fixation on a projected bright cross-hair on a dark background. The HCP website (https://www.humanconnectome.org/) provides the details of participants, the acquisition protocol and preprocessing of the functional data. Briefly, the fMRI data was preprocessed using standardized methods using FSL (FMRIB Software Library), FreeSurfer, and the Connectome Workbench software (Glasser et al., 2013; Smith et al., 2013). This preprocessing included correction for spatial and gradient distortions and head motion, intensity normalization and bias field removal, registration to the T1 weighted structural image, transformation to the 2mm Montreal Neurological Institute (MNI) space, using the FIX artefact removal procedure (Navarro Schroder et al., 2015; Smith et al., 2013). The head motion parameters were regressed out and structured artefacts were removed by ICA+FIX processing (Griffanti et al., 2014; Salimi-Khorshidi et al., 2014). Preprocessed timeseries of all grayordinates are in HCP CIFTI grayordinates standard space and available in the surface-based CIFTI file for each participant. A custom-made Matlab script, using the ft_read_cifti function from the Fieldtrip toolbox (Oostenveld et al., 2011), was used to extract the average timeseries of all the grayordinates in each region of the Schaefer parcellation, which are defined in the HCP CIFTI grayordinates standard space.

Structural connectivity using dMRI

Structural connectivity was estimated from diffusion spectrum and T2-weighted imaging data from 32 participants from the HCP database, scanned over 89 minutes. Acquisition parameters are described in detail in the HCP website (Setsompop et al., 2013). The freely available Lead-DBS software package (http://www.lead-dbs.org/) provided the preprocessing which is described in detail in Horn and colleagues (Horn et al., 2017) but, briefly, the data was processed using a generalized q-sampling imaging algorithm implemented in DSI studio (http://dsi-studio.labsolver.org). Segmentation of the T2-weighted anatomical images produced a white-matter mask and co-registering the images to the b0 image of the diffusion data using SPM12. In each HCP participant, 200,000 fibers were sampled within the white-matter mask. Fibers were transformed into MNI space using Lead-DBS (Horn and Blankenburg, 2016). We used the standardized methods in Lead-DBS to produce the structural connectomes for the Schaefer 1000 parcellation Scheme (Schaefer et al., 2018).

Schaefer parcellation

Schaefer and colleagues created a publicly available population atlas of cerebral cortical parcellation based on estimation from a large data set (n = 1489) (Schaefer et al., 2018). They provide parcellations of 400, 600, 800, and 1000 areas available in surface spaces, as well as MNI152 volumetric space. We used here the Schaefer parcellation with 1000 areas and estimated the Euclidean distances from the MNI152 volumetric space and extracted the timeseries from HCP using the HCP surface space version.

Data binarization

399   The rs-fMRI time-series were binarized to study the data statistics and to compared them to those
400   predicted by the spin model. For each scan, the z-scored time-series of each ROI, $z_i(t)$ ($1 \leq i \leq$
401   N), was binarized by imposing a threshold $\theta = 1$. The binarized activity was $\sigma_i(t) = 1$ if $z_i(t) >$
402   θ and $\sigma_i(t) = 0$ otherwise. Transformation of continuous signals into discrete point processes
403   has proven to effectively capture and compress fMRI large-scale dynamics (Tagliazucchi et al.,
404   2012). Importantly, the fluctuations that cross the threshold do not merely represent noise, since
405   the resulting point process largely overlaps with deconvoluted fMRI signals using the
406   hemodynamic response function and preserves the topology of the resting state networks
407   (Tagliazucchi et al., 2012). Furthermore, using maximum entropy models to estimate the
408   probability distribution of binarized activity, it has been shown that binarized rs-fMRI data is
409   poised close at a critical point (Ponce-Alvarez et al., 2022).

410

Correlation function

411

412   We calculated the average correlation $g(r)$ as a function of the Euclidean distance r between
413   ROIs. For this, we calculated the average correlation among pairs of nodes that were separated
414   by distances between r and $r + \Delta r$, with $\Delta r = 0.43$ mm, i.e.:

415
$$g(r) = \frac{1}{N_r} \sum_{r_{ij} \in [r, r+\Delta r]} c_{ij}, \quad (2)$$

416   where N_r is the number of pairs of ROIs (i, j) such that $r_{ij} \in [r, r + \Delta r]$, and r_{ij} and c_{ij} denote
417   the distance and the Pearson correlation between ROIs i and j, respectively. Distances between
418   ROIs range between 4.28 mm and 173.16 mm.

419

Phenomenological renormalization-group method

420

421   We here review the recently proposed PRG approach to study scale-invariance in neural systems
422   (Meshulam et al., 2019). Within this method, the collective activity is iteratively coarse-grained
423   by grouping together the variables that are maximally correlated.

424   Let $\sigma_i^{(0)}$ be the binary activity of ROI i for $i = 1, \dots, N$, with $\sigma_i^{(0)} \in \{0,1\}$. The superscript 0
425   indicates that the data is not coarse-grained. In the first coarse-graining step, we seek for the pair
426   of variables $\{i^*, j^*\}$ with maximal correlation and sum them:

427
$$\sigma_{i'}^{(1)} = \sigma_{i^*}^{(0)} + \sigma_{j^*}^{(0)}, \quad (3)$$

428   where $i' = 1, \dots, N/2$. We repeat this procedure for the second maximally correlated pair among
429   the remaining variables, i.e., from the set $\{i, j \in \{1, \dots, N\} : i, j \notin \{i^*, j^*\}\}$, and so on until all
430   pairs are used. This process is iterated for coarse-grained variables $\sigma_i^{(k)}$, resulting in clusters of
431   size $K = 2, 4, \dots, 2^k$. The size of the system is equal to $N_k = N/(2^k)$ at each coarse-graining step.

432 Along the coarse-graining procedure, several statistics of $\sigma_i^{(k)}$ are calculated and their change at
433 different coarse-graining steps are examined. A first observable is the variance of coarse-grained
434 variables:

$$V(K) = \frac{1}{N_k} \sum_{i=1}^{N_k} \langle \left(\sigma_i^{(k)} \right)^2 \rangle - \langle \sigma_i^{(k)} \rangle^2. \quad (4)$$

436 For calcium imaging recordings in the mouse hippocampus, it has been shown that the variance
437 scales with the cluster size, $V \propto K^{\tilde{\alpha}}$ (Meshulam et al., 2019), with a power-law exponent that lies
438 between linear ($\tilde{\alpha} = 1$) and quadratic growth ($\tilde{\alpha} = 2$), corresponding to uncorrelated and full-
439 correlated systems, respectively.

440 A second quantity is the probability of silence, $P_{\text{silence}}(K) = P(\sigma_i^{(k)} = 0)$ for all i. Assuming that
441 the probability distribution $P_K(\vec{\sigma}^{(k)})$ of the collective activity in a cluster of size K is a Boltzmann
442 distribution and that the configuration of complete silence has null energy, $P_{\text{silence}}(K)$ relates to
443 the partition function of the distribution, i.e., $P_{\text{silence}}(K) = Z_K^{-1}$. Thus $\ln P_{\text{silence}}(K)$ can be
444 associated to a free energy $F(K) = -\ln Z_K$. In calcium imaging recordings in the mouse
445 hippocampus, it has been shown that the free energy scales with the cluster size as $F \propto -K^{\tilde{\beta}}$
446 (Meshulam et al., 2018), with an exponent lower than 1, which is the expected value for
447 independent variables.

448 A third quantity is the spectrum of the covariance matrix inside a cluster of size K. Let λ denote
449 the eigenvalues of the covariance matrix. The eigenvalues are ordered from the highest
450 eigenvalue, rank $= 1$, to the lowest, rank $= K$. It has been shown that, at the fixed point of RG,
451 one expects that the eigen-spectrum scales with the relative rank (Meshulam et al., 2019):

$$\lambda \propto \left(\frac{\text{rank}}{K} \right)^{-\mu}. \quad (5)$$

453 In a D-dimensional system with translational invariance and a power-law correlation function
454 $g(r) \sim r^{-\tilde{\eta}}$ (as expected for a critical system), the exponent μ is related to $\tilde{\eta}$. In this case, the
455 eigenvalues are given by the Fourier transform of the correlation function (Vinayak et al., 2014):

$$\lambda(\vec{k}) = \int d^D r \, g(r) e^{i\vec{k}.\vec{r}} \sim \frac{1}{|\vec{k}|^{D-\tilde{\eta}}}. \quad (6)$$

457 Since the rank scales as rank$\sim |\vec{k}|^D$, one has: $\mu = (D - \tilde{\eta})/D$. However, the $\tilde{\eta}$ exponent does not
458 satisfy this relation neither in the critical spin model nor in the fMRI data. This might indicate
459 that the system is not translational invariant.

460

461 **Whole-brain spin model**

462 To relate the observed fMRI statistics to critical dynamics, we built a spin model based on large-
463 scale connectivity. In this model, the state of each node is described by a binary variable or "spin",
464 i.e., $\sigma_i \in [-1, +1]$, and the collective activity of the N nodes is given by a binary pattern or

465   configuration $\vec{\sigma} = [\sigma_1, \dots, \sigma_N]$. The probability of each pattern is given by the Boltzmann
466   distribution:

$$P(\vec{\sigma}) = \frac{1}{Z}\exp[-E(\vec{\sigma})], \quad (7)$$

468   where $E(\vec{\sigma})$ represents the energy of the pattern and is given as:

$$E(\vec{\sigma}) = -\beta \sum_{i,j} C_{ij}\sigma_i\sigma_j. \quad (8)$$

470   Z is the partition function, i.e., $Z = \sum_{\{\vec{\sigma}\}} \exp(-E(\vec{\sigma}))$. Spins interact through the connectivity
471   matrix $\boldsymbol{C}$. β is a scaling parameter of the connectivity matrix $\boldsymbol{C}$; it is equivalent to an inverse
472   temperature, i.e., $\beta = 1/T$, which is the free parameter of the model.

473   For each configuration $\vec{\sigma}$, the population activity is defined as the average node value: $M(\vec{\sigma}) =$
474     $\sum_i \sigma_i/N$. The average population activity $\langle M \rangle$ was obtained by averaging across simulation steps.
475   The model presents a second-order phase transition that can be detected by examining the
476   behavior of $\langle M \rangle$ as a function of the temperature parameter. For temperatures lower than a critical
477   value, $T_c = \beta_c^{-1}$, the spin model presents a spontaneous population activity, i.e., $|\langle M \rangle| > 0$
478   (subcritical regime), that vanishes for temperatures larger than T_c (supercritical regime).

479   Realizations of the spin model were obtained using Monte Carlo Metropolis simulations. The
480   algorithm starts with an initial random configuration of N spins, then flips the spin of a randomly
481   chosen node, and calculates the change in energy ΔE induced by the spin flip. If $\Delta E < 0$, the spin
482   flip is accepted, otherwise it is accepted with probability $\exp(-\beta\Delta E)$. For each tested value of
483   β, we ran 5 realizations (with different initial conditions) of $50{,}000 \times N$ simulation steps. The
484   system's configuration was stored every N flip attempts. To avoid dependences on initial
485   conditions, simulations started with extra 500,000 steps without storing the configurations. The
486   population activity, the correlation function, the coarse-grained variance, and the coarse-grained
487   eigen-spectrum were averaged over realizations, for each β.

488

References

490   Beggs, J.M. & Plenz, D. Neuronal avalanches in neocortical circuits. *J. Neurosci.* **23**, 11167-
491   11177 (2003).

492   Biswal, B., Yetkin, F.Z., Haughton, V.M. & Hyde, J.S. Functional connectivity in the motor
493   cortex of resting human brain using echo-planar MRI. *Magn. Reason. Med.* **34**, 537-541 (1995).

494   Chang, C. & Glover, G.H. Time-frequency dynamics of resting-state brain connectivity
495   measured with fMRI. *NeuroImage* **50**, 81-98 (2010).

496   Choi, H. & Mihalas, S. Synchronization dependent on spatial structures of a mesoscopic whole-
497   brain network. *PLoS Comput. Biol.* **15**, e1006978 (2019).

498   Ciuciu, P., Varoquaux, G., Abry, P., Sadaghiani, S. & Kleinschmidt, A. Scale-free and
499   multifractal time dynamics of fMRI signals during rest and task. *Front. Physiol.* **3**, 186 (2012).

500   Cocchi, L., Gollo, L.L., Zalesky, A. & Breakspear, M. Criticality in the brain: A synthesis of
501   neurobiology, models and cognition. *Prog. in Neurobiol.* **158**, 132-152 (2017).

502   Deco, G. *et al*. Rare long-range cortical connections enhance human information processing.
503   *Curr Biol.* **31**, 4436-4448 (2021).

504   Dehghani, N., Bédard, C., Cash, S.S., Halgren, E. & Destexhe, A. Comparative power spectral
505   analysis of simultaneous electroencephalographic and magnetoencephalographic recordings in
506   humans suggests non-resistive extracellular media: EEG and MEG power spectra. *J. Comput.*
507   *Neurosci.* **29**, 405 (2010).

508   di Santo, S., Villegas, P., Burioni, R. &Muñoz, M.A. Landau–Ginzburg theory of cortex
509   dynamics: Scale-free avalanches emerge at the edge of synchronization. *Proc. Natl. Acad. Sci.*
510   *USA* **115**, e1356-e1365 (2018).

511   Ercsey-Ravasz, M. *et al*. A predictive network model of cerebral cortical connectivity based on
512   a distance rule. *Neuron* **80**, 184-197 (2013).

513   Ezaki, T. *et al.* Closer to critical resting-state neural dynamics in individuals with higher fluid
514   intelligence. *Commun Biol* **3**, 52 (2020).

515   Fekete, T. *et al*. Critical dynamics, anesthesia and information integration: Lessons from multi-
516   scale criticality analysis of voltage imaging data. *NeuroImage* **183**, 919-933 (2018).

517   Fox, M.D. & Raichle, M.E. Spontaneous fluctuations in brain activity observed with functional
518   magnetic resonance imaging. *Nat. Rev. Neurosci.* **8**, 700-711 (2007).

519   Friedman, N. *et al*. Universal Critical Dynamics in High Resolution Neuronal Avalanche Data.
520   *Phys. Rev. Lett.* **108**, 208102 (2012).

521   Glasser, M.F. *et al*. The minimal preprocessing pipelines for the Human Connectome Project.
522   *NeuroImage* **80**, 105-124 (2013).

523   Griffanti, L. *et al*. ICA-based artefact removal and accelerated fMRI acquisition for improved
524   resting state network imaging. *NeuroImage* **95**, 232-247 (2014).

525   Hahn, G. *et al*. Neuronal avalanches in spontaneous activity in vivo. *J. Neurophysiol.* **104**,
526   3312-3322 (2010).

527   Hahn, G. *et al*. Spontaneous cortical activity is transiently poised close to criticality. *PLoS*
528   *Comput. Biol.* **13**, e1005543 (2017).

529   He, B.J. Scale-free properties of the functional magnetic resonance imaging signal during rest
530   and task. *J. Neurosci.* **31**, 13786-13795 (2011).

531   He, B.J., Zempel, J.M., Snyder, A.Z. & Raichle, M.E. The temporal structures and functional
532   significance of scale-free brain activity. *Neuron* **66**, 353-369 (2010).

533   Hesse, J. & Gross, T. Self-organized criticality as a fundamental property of neural systems.
534   *Front. Syst. Neurosci.* **8**, 166 (2014).

535 Hobbs, J.P., Smith, J.L. & Beggs, J.M. Aberrant neuronal avalanches in cortical tissue removed
536 from juvenile epilepsy patients. *J. Clin. Neurophysiol.* **27**, 380-386 (2010).

537 Horn, A. & Blankenburg, F. Toward a standardized structural-functional group connectome in
538 MNI space. *NeuroImage* **124**, 310-322 (2016).

539 Horn, A., Neumann, W.J., Degen, K., Schneider, G.H. & Kuhn, A.A. Toward an
540 electrophysiological "sweet spot" for deep brain stimulation in the subthalamic nucleus. *Hum.*
541 *Brain Mapp.* **38**, 3377-3390 (2017).

542 Horvát, S. *et al*. Spatial embedding and wiring cost constrain the functional layout of the
543 cortical network of rodents and primates. *PLoS Biol.* **14**, e1002512 (2016).

544 Knox, J. *et al*. High-resolution data-driven model of the mouse connectome. *Netw. Neurosci.* **3**,
545 217-236 (2018).

546 Marinazzo, D. *et al*. Information transfer and criticality in the Ising model on the human
547 connectome. *PLoS One* **9**, e93616 (2014).

548 Markov, N.T. *et al*. Weight consistency specifies regularities of macaque cortical networks.
549 *Cereb. Cortex* **21**, 1254-1272 (2011).

550 Markov, N.T. *et al*. A weighted and directed interareal connectivity matrix for macaque cerebral
551 cortex. *Cereb. Cortex* **24**, 17-36 (2012).

552 Markov, N.T. *et al*. The role of long-range connections on the specificity of the macaque
553 interareal cortical network. *Proc. Natl. Acad. Sci. USA* **110**, 5187-5192 (2013).

554 Massobrio, P., de Arcangelis, L., Pasquale, V., Jensen, H.J. & Plenz, D. Criticality as a
555 signature of healthy neural systems. *Front. Syst. Neurosci.* **9**, 22 (2015).

556 Meisel, C., Storch, A., Hallmeyer-Elgner, S., Bullmore, E. & Gross, T. Failure of adaptive self-
557 organized criticality during epileptic seizure attacks. *PLoS Comput. Biol.* **8**, e1002312 (2012).

558 Meshulam, L., Gauthier, J.L., Brody, C.D., Tank, D.W. & Bialek, W. Coarse graining, fixed
559 points, and scaling in a large population of neurons. *Phys. Rev. Lett.* **123**, 178103 (2019).

560 Meshulam, L., Gauthier, J.L., Brody, C.D., Tank, D.W. & Bialek, W. Coarse-graining and hints
561 of scaling in a population of 1000+ neurons. *arXiv*, 1812.11904 (2018).

562 Milstein, J., Mormann, F., Fried, I., & Koch, C. Neuronal shot noise and Brownian $1/f^2$
563 behavior in the local field potential. *PLoS ONE* **4**, e4338 (2009).

564 Navarro Schroder, T., Haak, K.V., Zaragoza Jimenez, N.I., Beckmann, C.F. & Doeller, C.F.
565 Functional topography of the human entorhinal cortex. *eLife* **4** (2015).

566 Nicoletti, G., Suweis, S. & Maritan, A. Scaling and criticality in a phenomenological
567 renormalization group. *Phys. Rev. Res.* **2**, 023144 (2020).

568 Oostenveld, R., Fries, P., Maris, E. & Schoffelen, J.M. FieldTrip: Open source software for
569 advanced analysis of MEG, EEG, and invasive electrophysiological data. *Comput. Intell.*
570 *Neurosci.* **2011**, 156869 (2011).

571 Palva, J.M. *et al*. Neuronal long-range temporal correlations and avalanche dynamics are
572 correlated with behavioral scaling laws. *Proc. Natl. Acad. Sci. USA* **110**, 3585-3590 (2013).

573 Pasquale, V., Massobrio, P., Bologna, L.L., Chiappalone, M. & Martinoia, S. Self-organization
574 and neuronal avalanches in networks of dissociated cortical neurons. *Neuroscience* **153**, 1354-
575 1369 (2008).

576 Ponce-Alvarez, A., Jouary, A., Privat, M., Deco, G. & Sumbre, G. Whole-brain neuronal
577 activity displays crackling noise dynamics. *Neuron* **100**, 1446-1459 (2018).

578 Ponce-Alvarez, A. *et al*. Macroscopic quantities of collective brain activity during wakefulness
579 and anesthesia. *Cereb. Cortex* **32**, 298-311 (2022).

580 Ribeiro, T.L *et al*. Spike avalanches exhibit universal dynamics across the sleep-wake cycle.
581 *PLoS ONE* **5**, e14129 (2010).

582 Rocha, R.P. *et al*. Recovery of neural dynamics criticality in personalized whole-brain models
583 of stroke. *Nat. Comm.* **13**, 3683 (2022).

584 Rubinov, M., Ypma, R., Watson, C. & Bullmore, E. Wiring cost and topological participation of
585 the mouse brain connectome. *Proc. Natl. Acad. Sci. USA* **112**, 10032-10037 (2015).

586 Salimi-Khorshidi, G. *et al*. Automatic denoising of functional MRI data: combining independent
587 component analysis and hierarchical fusion of classifiers. *NeuroImage* **90**, 449-468 (2014).

588 Schaefer, A. *et al*. Local-Global Parcellation of the Human Cerebral Cortex from Intrinsic
589 Functional Connectivity MRI. *Cerebral cortex* **28**, 3095-3114 (2018).

590 Setsompop, K. *et al*. Pushing the limits of in vivo diffusion MRI for the Human Connectome
591 Project. *NeuroImage* **80**, 220-233 (2013).

592 Shew, W.L., Yang, H., Petermann, T., Roy, R. & Plenz, D. Neuronal avalanches imply maximum
593 dynamic range in cortical networks at criticality. *J. Neurosci.* **29**, 15595-600 (2009).

594 Shew, W.L. & Plenz, D. The functional benefits of criticality in the cortex. *Neuroscientist* **19**, 88-
595 100 (2013).

596 Shriki, O. *et al*. Neuronal Avalanches in the Resting MEG of the Human Brain. *J. Neurosci.* **33**,
597 7079-7090 (2013).

598 Smith, S.M. *et al*. Resting-state fMRI in the Human Connectome Project. *NeuroImage* **80**, 144-
599 168 (2013).

600 Sotiropoulos, S.N. & Zalesky, A. Building connectomes using diffusion MRI: why, how and
601 but. *NMR biomed.* **32**, e3752 (2019).

602 Tagliazucchi, E., Balenzuela, P., Fraiman, D. & Chialvo, D.R. Criticality in large-scale brain
603 fMRI dynamics unveiled by a novel point process analysis. *Front. Physiol.* **3**, 15 (2012).

604 Tagliazucchi, E. *et al*. Large-scale signatures of unconsciousness are consistent with a departure
605 from critical dynamics. *J. R. Soc. Interface* **13**, 20151027 (2016).

606 Theodoni, P. *et al*. Structural attributes and principles of the neocortical connectome in the
607 marmoset monkey. *Cereb. Cortex* **32**, 15-28 (2022).

608 Tinker, J. & Perez Velazquez, J.L. Power law scaling in synchronization of brain signals
609 depends on cognitive load. *Front. Syst. Neurosci.* **8**, 73, (2014).

610 Vinayak, S., Prosen, T., Buča, B. & Seligman, T.H. Spectral analysis of finite-time correlation
611 matrices near equilibrium phase transitions. *EPL* **108**, 20006 (2014).